Geophysical Research Letters

RESEARCH LETTER
10.1029/2022GL099411

# Single-Crystal Elasticity of Antigorite at High Pressures and Seismic Detection of Serpentinized Slabs

**Niccolò Satta[1,2], Luiz Fernando Grafulha Morales[3,4], Giacomo Criniti[1], Alexander Kurnosov[1], Tiziana Boffa Ballaran[1], Sergio Speziale[5], Katharina Marquardt[6], Gian Carlo Capitani[7], and Hauke Marquardt[2]**

[1]Bayerisches Geoinstitut, University of Bayreuth, Bayreuth, Germany, [2]Department of Earth Sciences, University of Oxford, Oxford, UK, [3]Scientific Center for Optical and Electron Microscopy, ETH Zürich, Zürich, Switzerland, [4]Structural Geology and Tectonics group, Geological Institute, Department of Earth Sciences - ETH Zürich, Zürich, Switzerland, [5]German Research Centre for Geosciences GFZ, Potsdam, Germany, [6]Department of Materials, Faculty of Engineering, Imperial College London, London, UK, [7]Department of Earth and Environmental Sciences, University of Milano-Bicocca, Milano, Italy

**Abstract** The subduction of serpentinized slabs is the dominant process to transport "water" into Earth's mantle, and plays a pivotal role for subduction dynamics. Antigorite, the most abundant serpentine mineral in subduction settings, may imprint a seismic signature on serpentinized slabs, making them seismically distinguishable from the dry, non-serpentinized ones. However, the complete single-crystal elasticity of antigorite has not been experimentally constrained at high pressures, hindering the use of seismological approaches to detect serpentinization in subducting slabs. Here, we report the full elastic stiffness tensor of antigorite by single-crystal Brillouin spectroscopy and X-ray diffraction up to 7.71(5) GPa. We use our results to model seismic properties of antigorite-bearing rocks and show that their seismological detectability depends on the geometrical relation between seismic wave paths and foliation of serpentinized rocks. In particular, we demonstrate that seismic shear anisotropy shows low sensitivity to serpentinization for a range of relevant geometries.

**Plain Language Summary** The subduction of serpentinized slabs plays a key role in the deep recycling of water into the Earth's interior. Antigorite is the main serpentine mineral in subducting slabs, and the most important carrier of water. Antigorite-bearing rocks are predicted to have a distinct seismic signature, potentially allowing them to be detected with seismological approaches. However, our current knowledge on seismic properties of antigorite-bearing rocks is limited, mostly hampered by a lack of experimental constraints on single-crystal elasticity of antigorite at relevant pressures. In this study, state-of-the-art techniques were employed to produce the first experimental description of the complete high-pressure elasticity of antigorite single crystals. Our experimental data set was implemented in the modeling of seismic properties of antigorite-bearing rocks at pressures relevant for subduction. Our results were used to discuss the relation between seismic wave path and shear wave anisotropy in serpentinized slabs, and challenge the use of shear wave splitting as a proxy for serpentinization in slabs.

**Key Points:**

- Single-crystal elasticity of antigorite at high pressures is determined by Brillouin spectroscopy and X-ray diffraction experiments
- Seismic signature of serpentinized slabs is constrained in a relevant composition-pressure space
- Serpentinization in slabs may be undetectable through shear wave anisotropy

**Supporting Information:**

Supporting Information may be found in the online version of this article.

**Correspondence to:**

N. Satta,
niccolo.satta@earth.ox.ac.uk

**Citation:**

Satta, N., Grafulha Morales, L. F., Criniti, G., Kurnosov, A., Boffa Ballaran, T., Speziale, S., et al. (2022). Single-crystal elasticity of antigorite at high pressures and seismic detection of serpentinized slabs. *Geophysical Research Letters*, *49*, e2022GL099411. https://doi.org/10.1029/2022GL099411

Received 9 MAY 2022
Accepted 15 JUL 2022



## 1. Introduction

Water ($H_2O$) influences the physical properties of Earth's mantle (Ohtani, 2020). Therefore, understanding the deep recycling of water is crucial in describing global-scale geological processes (Faccenda, 2014). Water is primarily delivered into the convecting mantle by the subduction of hydrated oceanic plates, that is, slabs (Rupke, 2004). The hydration of slabs occurs through serpentinization (Faccenda et al., 2009), a process involving the alteration of ultramafic minerals to form serpentines (Moody, 1976). Serpentinization is expected to mostly take place along faults fracturing the lithosphere prior to subduction (Ranero et al., 2003). When bending beneath the overriding plate, slabs may develop a network of normal faults that can lead to the formation of km-sized, serpentinite-bearing bodies within the lithospheric portion of the slab (Faccenda et al., 2008, 2009; Sibson, 2000). Direct evidence for this process can be detected, for example, in slabs subducting offshore of Central and South America (Contreras-Reyes et al., 2008; Ranero & Sallarès, 2004), and Tonga (Contreras-Reyes et al., 2011).

Antigorite is the serpentine mineral stable at high pressures and temperatures, hence it is the most abundant serpentine in altered (serpentinized) slabs (Schwartz et al., 2013). Previous studies suggest that antigorite in subducting slabs may break down at relatively low depths, resulting in a discharge of upward migrating fluids, which might contribute to the further serpentinization of the mantle wedge (DeShon & Schwartz, 2004), as well as triggering arc magmatism (Schmidt & Poli, 1998) and episodic tremor (Campione & Capitani, 2013; Ferrand et al., 2017; Kaproth & Marone, 2013). In relatively cold subduction settings, however, antigorite may be preserved in the slab interior up to about 180 km depth, playing a key role in recycling water and other volatiles by carrying them to the deep Earth's mantle (Frost, 1999; Krantz et al., 2019; Ulmer & Trommsdorff, 1995), a process supported by the analysis of diamond inclusions (Smith et al., 2021). Therefore, mapping the distribution of antigorite-bearing rocks within subducting slabs becomes pivotal to evaluate different scenarios, and quantify the deep recycling of water and other volatiles in subduction zones.

Antigorite crystalizes in the monoclinic system, and its main structural features are sinusoidal-like 1:1 layers of octahedrally and tetrahedrally coordinated cation sites stacked perpendicularly to the (001) basal plane (Figure S1a in Supporting Information S1; Capitani & Mellini, 2004, 2006). Specifically, octahedra share edges with each other, while tetrahedra are connected via their vertices to form a pseudo-hexagonal ring arrangement with a periodic polarity reversal (Figure S1b in Supporting Information S1; Capitani & Mellini, 2005). Previous computational (Mookherjee & Capitani, 2011) and experimental investigations (Bezacier et al., 2010, 2013; Marquardt et al., 2015) reported antigorite single crystals to be relatively stiff along directions within the basal plane, but very compressible perpendicular to it. Thus, antigorite single crystals show an important elastic anisotropy at room pressure, where the shear waves polarized parallel to the layering are twice as fast as those polarized perpendicular to it (Bezacier et al., 2010). Importantly, serpentine minerals in subduction zones are expected to accommodate most of the deformation due to their relatively weak mechanical strength (Escartín et al., 1997, 2001; Hirth & Guillot, 2013). Thus, the development of a crystallographic preferred orientation (CPO) is expected in antigorite, with crystallites aligning their (001) basal plane parallel to the flow deformation plane, as found in naturally and experimentally deformed serpentine-bearing samples (Katayama et al., 2009; Kern et al., 1997; Morales et al., 2013; Padrón-Navarta et al., 2012). The combination of a marked CPO with a large elastic anisotropy makes antigorite a strong candidate to explain the seismic shear wave anisotropy observed in subduction zones. In subducting slabs, antigorite-bearing rocks are predicted to eventually align their foliation vertically and parallel to the trench, as the slab rotates around an axis parallel to the trench line during subduction (Faccenda et al., 2008). Therefore, seismic waves traveling vertically and parallel along slabs may be sampling antigorite-bearing rocks in a direction parallel to foliation, possibly causing shear wave delay times in the order of seconds (Faccenda et al., 2008) and potentially making serpentinized slabs the major contributor to the delay times in shear waves observed in many subduction zones (Long & Silver, 2008). However, the single-crystal elastic stiffness tensor of antigorite has not yet been fully constrained at high pressures, and previous models largely rely on either room pressure measurements (Bezacier et al., 2010) or theoretical predictions (Mookherjee & Capitani, 2011).

In this study, and for the first time, the complete elastic stiffness tensor of antigorite single crystals was derived experimentally at high pressures. Our results are based on X-ray diffraction (XRD) and Brillouin spectroscopy measurements performed on two oriented, double-side polished single-crystal platelets of natural antigorite, that were pressurized simultaneously in a diamond-anvil cell (DAC) up to 7.71(5) GPa. The elasticity data set obtained in the present work was combined with previously determined crystallographic textures and microstructural information to model seismic properties of deformed antigorite-bearing rocks. Seismic properties at relevant pressure conditions were characterized in terms of the degree of serpentinization, that is, antigorite fraction, and pressure. Our model indicates that low serpentinization degrees, and/or particular geometrical relations between seismic wave propagation and antigorite foliation, may result in antigorite-bearing rocks showing low shear wave splitting, making them indistinguishable from dry, non-serpentinized rocks. Our findings provide new bounds on the seismic detectability on serpentinization in slabs, further suggesting that considering seismic wave paths is crucial to accurately map antigorite-bearing rocks in slabs through the interpretation of seismic anisotropy.

## 2. Materials and Methods

Samples investigated in this study belong to the MG 159 antigorite specimen extracted from the Malenco serpentinite body. A comprehensive description of the geological framework, and sampling details of the MG 159 antigorite specimen are available in Mellini et al. (1987). According to Capitani & Mellini (2006), the chemical formula for the MG159 samples is:

$$\left(Mg_{2.638}Fe_{0.102}Al_{0.047}Cr_{0.014}Ni_{0.003}Mn_{0.002}\right)_{\Sigma=2.808}\left(Si_{1.971}Al_{0.029}\right)_{\Sigma=2}O_5(OH)_{3.647}$$

Two samples, namely X1 and X2, were selected from a batch of MG 159 single crystals based on the sharpness of their optical extinction. Selected single crystals were subsequently oriented along chosen crystallographic planes (Text S1 in Supporting Information S1), and double-side polished to a final thickness of 25 (X1) and 15 μm (X2), respectively. In a Cartesian reference system ($e_1$, $e_2$, $e_3$) with $e_2 \| \mathbf{b}$ and $e_3 \| \mathbf{c}$, the orientations in fractional coordinates of X1 and X2 platelets are (−0.131, 0.022, 0.991) and (0.467, 0.808, −0.359), respectively.

### 2.1. High-Pressure Experiments

High-pressure experiments were conducted employing a BX90 DAC (Kantor et al., 2012) equipped with 500 μm culet size Boehler-Almax Ia-type diamonds (Boehler & De Hantsetters, 2004). A circular sample chamber with a diameter of 370 μm was laser-cut in a rhenium foil pre-indented to a thickness of 60 μm. Sample loading was performed following a multi-loading strategy (Figure S2 in Supporting Information S1; Schulze et al., 2017). A ruby sphere was used for *in-situ* pressure determination ($P_{ruby}$) using the ruby fluorescence scale (Dewaele et al., 2004). Ruby fluorescence spectra were collected on the pressurized ruby before and after each experiment. Helium was employed as pressure-transmitting medium as it remains hydrostatic in the investigated pressure range (Klotz et al., 2009). Gas loading was performed using the facility at the Bayerisches Geoinstitut (BGI), University of Bayreuth (Kurnosov et al., 2008).

High-pressure XRD and Brillouin spectroscopy experiments were conducted at the BGI using the Xcalibur diffractometer and the Brillouin spectroscopy system, respectively. Technical details on these two systems are provided in Text S2 in Supporting Information S1, and in Trots et al. (2013).

The elastic stiffness tensor of antigorite is defined by thirteen independent, non-zero elastic stiffness coefficients ($c_{ij}$) that in Voigt notation (Nye, 1985) are: $c_{11}$, $c_{22}$, $c_{33}$, $c_{44}$, $c_{55}$, $c_{66}$, $c_{12}$, $c_{13}$, $c_{23,}$ $c_{15}$, $c_{25}$, $c_{35}$, $c_{46}$. At each of the investigated pressure points, compressional ($v_P$), fast shear ($v_{S1}$) and slow shear ($v_{S2}$) wave velocities determined for both platelets were inverted together with the platelet orientations and density in a weighted nonlinear least-square fitting of the Christoffel equation (Haussühl, 2007):

$$|c_{ijkl}n_jn_l - \rho v^2\delta_{ik}| = 0 \quad (1)$$

where $c_{ijkl}$ are the elastic stiffness coefficients in tensorial notation, $n_jn_l$ the phonon direction cosines, $\rho$ the density and $\delta_{ik}$ the Kronecker delta. Density is calculated using the unit-cell volumes ($V$) resulting from XRD experiments, and using the molar mass constrained by previous studies (Capitani & Mellini, 2004, 2006). The best-fitting $c_{ij}$ (Table S1 in Supporting Information S1) were used to calculate Voigt and Reuss bounds (labeled with V and R superscripts, respectively, Table S2 in Supporting Information S1) for the isotropic aggregate $K_S$ and shear $G$ moduli. This was done using an OriginPro (OriginLab corporation, USA) script employing the equations coded in POLYXSTAL (Watt, 1987). The Hill averaged values (superscripted H, Table S2 in Supporting Information S1) were then determined as the arithmetic mean of Voigt and Reuss bounds (Hill, 1952).

## 3. Results and Discussion

High-pressure XRD and Brillouin spectroscopy experiments were performed at 8 different pressures, and up to 7.71(5) GPa. A typical Brillouin spectrum is provided in Figure S3 in Supporting Information S1. Observed and calculated acoustic wave velocities collected for both platelets at 7.71(5) GPa versus the rotation angle $\chi$ are shown in Figure S4 in Supporting Information S1.

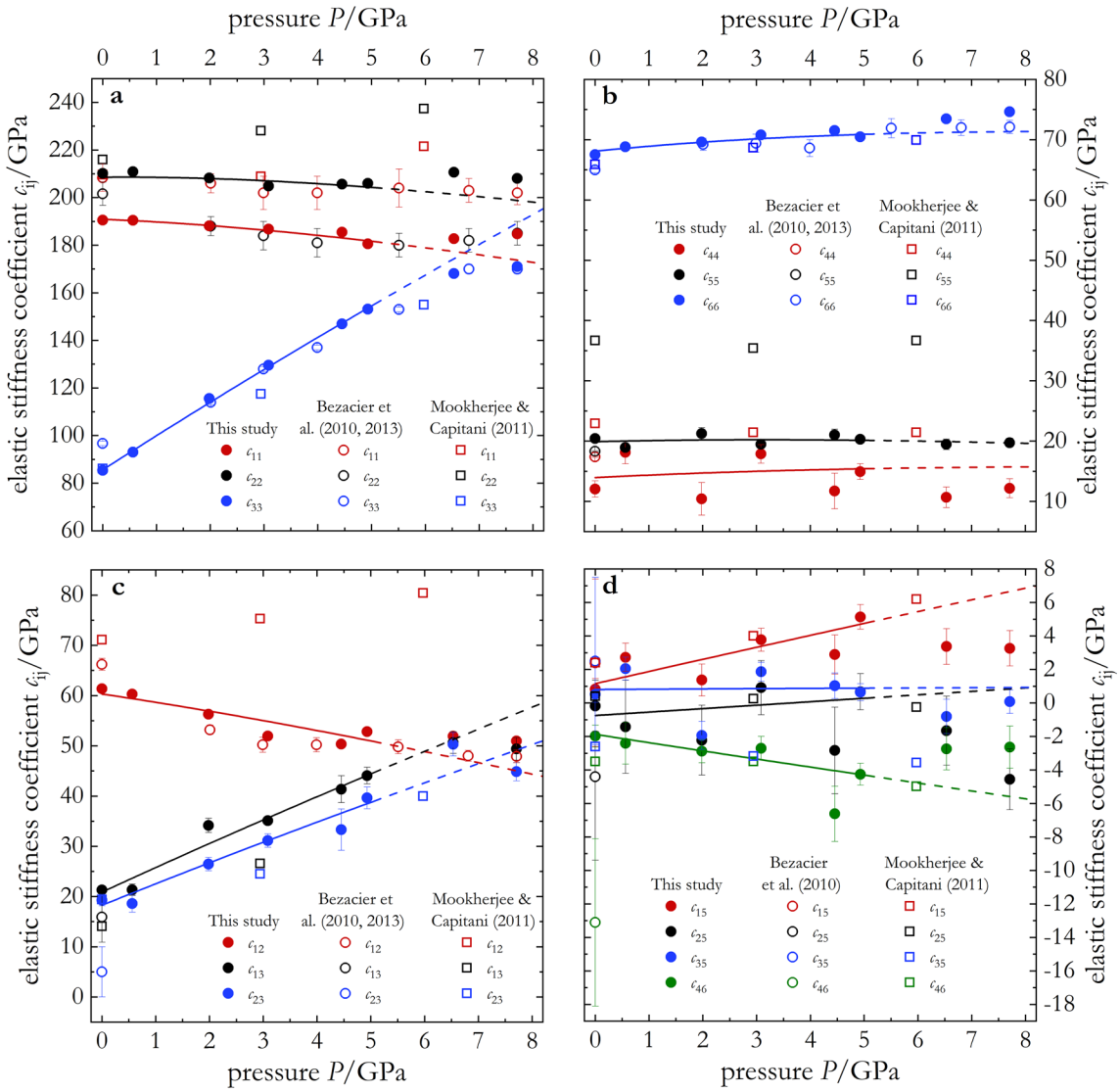


**Figure 1.** Single-crystal elastic stiffness coefficients ($c_{ij}$) of antigorite. Solid symbols are $c_{ij}$ constrained in this study; open symbols are literature data. Note that only $c_{11}$, $c_{22}$, $c_{33}$, $c_{66}$ and $c_{12}$ were constrained by Bezacier et al. (2013) at high pressures. Solid lines are fits to our data up to $P_{ruby}$ = 5.17 GPa using 3rd-order finite strain equations (Text S3 in Supporting Information S1). Dashed lines are extrapolations of the fitted curves to larger pressures.

### 3.1. Single-Crystal Elasticity of Antigorite

At room pressure, we find the $c_{11,0}$ and $c_{22,0}$ (where the subscript 0 refers to room pressure) to have a similar magnitude, both exhibiting values about twice that of $c_{33,0}$ (Figure 1a). Also, $c_{44,0}$ and $c_{55,0}$ are three and four times smaller than $c_{66,0}$, respectively (Figure 1b). Moreover, we find $c_{12,0}$ to be about three times larger than $c_{13,0}$ and $c_{23,0}$ (Figure 1c). On the other hand, $c_{15,0}$, $c_{25,0}$, $c_{35,0}$ and $c_{46,0}$ are relatively small in terms of magnitude, that is, <2 GPa (Figure 1d). In general, our results at room pressure are in good agreement with previous theoretical predictions of static (0 K) elastic properties based on the Generalized Gradient Approximation (GGA) (Mookherjee & Capitani, 2011; Mookherjee & Steinle-Neumann, 2009a, 2009b) and Brillouin spectroscopy investigations (Bezacier et al., 2010). Specifically, all $c_{ij}$ determined in this study are essentially identical in terms of absolute values to those predicted by GGA, except for $c_{55,0}$ and $c_{44,0}$, which are about twice than those determined in this study. The main difference with respect to the study of Bezacier et al. (2010) is that $c_{11,0} > c_{22,0}$. However we note that this discrepancy is likely due to the misassignment by Bezacier et al. (2010) of the mentioned $c_{ij,0}$ to the *a*- and *b*-axes (Marquardt et al., 2015).

**Table 1**
*Room Pressure Elastic Stiffness Coefficients ($c_{ij,0}$) of Antigorite and Isotropic Aggregate Elastic Moduli ($M_{S0}$), Together With Their First Pressure Derivatives ($c'_{ij,0}$ and $M'_{S0}$, Respectively) Determined in This Study*

| ij | $c_{ij,0}$/GPa | $c'_{ij,0}$ | | $M_{S0}$/GPa | $M'_{S0}$ |
|---|---|---|---|---|---|
| 11 | 191(1.1) | −0.7(3) | | | |
| 22 | 209(1) | 0.2(2) | | Voigt Bound | |
| 33 | 85.6(12) | 11.8(3) | $K^V_{S0}$ | 76.0(7) | 2.6(2) |
| 44 | 14(3) | 0.4(7) | $G^V_{S0}$ | 46.1(7) | 0.6(2) |
| 55 | 19.9(10) | 0.2(3) | | | |
| 66 | 68.1(4) | 0.7(5) | | Reuss Bound | |
| 12 | 60.3(8) | −1.3(2) | $K^R_{S0}$ | 62.1(10) | 5.7(4) |
| 13 | 21(2) | 4.0(6) | $G^R_{S0}$ | 30(2) | 0.4(5) |
| 23 | 18(2.5) | 3.5(9) | | | |
| 15 | 1.2(13) | 0.6(4) | | Hill Average | |
| 25 | −1(3) | 0.2(7) | $K^H_{S0}$ | 69.1(6) | 4.0(2) |
| 35 | 0.8(10) | 0.0(3) | $G^H_{S0}$ | 38.3(10) | 0.5(3) |
| 46 | −1.9(14) | −0.4(4) | | | |

*Note.* Parameters listed here are obtained by fitting 3rd-order Eulerian strain equations to high-pressure data and up to 5.17(2) GPa (Text S3 in Supporting Information S1, Stixrude & Lithgow-Bertelloni, 2005).

We employed 3rd-order Eulerian strain equations (Text S3 in Supporting Information S1, Stixrude & Lithgow-Bertelloni, 2005) to describe the variation with pressure of individual $c_{ij}$. Only experimental data collected at $P_{ruby} \leq 5.17(2)$ GPa were employed in the fitting procedure as antigorite has been found to display elastic anomalies at pressures of about 6.5 GPa (Bezacier et al., 2013; Marquardt et al., 2015; Nestola et al., 2010). The parameters resulting from the fit are listed in Table 1, and fits to the observed $c_{ij}$ are plotted against the absolute pressure (Text S4 in Supporting Information S1) in Figure 1. Within the considered pressure range ($P_{ruby} < 5.17(2)$ GPa), our results are in agreement with previous Brillouin spectroscopy investigations (Bezacier et al., 2013), except for the $c_{11}$–$c_{22}$ mismatch, as already observed in the room pressure data. Note that only $c_{11}$, $c_{22}$, $c_{33}$, $c_{66}$ and $c_{12}$ were actually constrained by Bezacier et al. (2013) at high pressures. In contrast, we see only partial agreement with previous GGA estimates, as these did not predict any softening of $c_{11}$, $c_{22}$ and $c_{12}$ in the pressure range considered in this study, although they predicted it to occur at larger pressures (Mookherjee & Capitani, 2011). At relatively low pressures ($P < 6$ GPa), the compression mechanism of antigorite is expected to be governed by a reduction of the interlayer distance, together with the flattening of octahedral and tetrahedral layers, improving the geometrical match between these two structural units (Capitani & Stixrude, 2012). Therefore, it is likely that the softening exhibited by $c_{11}$, $c_{22}$ and $c_{12}$ is coupled to the reduction of the geometrical mismatch between layers upon compression, while the shortening of interlayer distance likely causes the abrupt stiffening of $c_{33}$, $c_{13}$ and $c_{23}$.

Extrapolation of the 3rd-order Eulerian strain equation fits to larger pressures shows that at least a subset of the $c_{ij}$, for example, $c_{11}$ and $c_{33}$, deviates from the low-pressure behavior (Figure 1), suggesting the presence of anomalies in the elastic behavior of antigorite as previously experimentally detected in acoustic wave velocities (Bezacier et al., 2013; Marquardt et al., 2015), and unit-cell volume compression at pressures of about 6.5 GPa (Nestola et al., 2010). We speculate that the observed deviation may reflect a change in the compression mechanism of antigorite, as predicted by Capitani & Stixrude (2012) occurring at about 6 GPa. Specifically, the compression mechanism of antigorite is expected to evolve from being primarily dominated by a shortening of the interlayered distance and a flattening of the sinusoidal-like layers ($P < 6$ GPa), to being essentially controlled by ditrigonalization, that is, in-plane rotation of the tetrahedra at pressures between 6 and 20 GPa (Capitani & Stixrude, 2012).

### 3.2. Isotropic Aggregate Properties of Antigorite

The isotropic aggregate properties of antigorite calculated for each of the investigated pressure points are listed in Table S2 in Supporting Information S1, and plotted against absolute pressure in Figure 2. At room pressure, the Hill averaged value of adiabatic bulk ($K^H_{S0}$) and shear ($G^H_{S0}$) moduli are identical within uncertainties to those determined by previous Brillouin spectroscopy experiments (Bezacier et al., 2010), and broadly consistent with GGA predictions (Mookherjee & Capitani, 2011). At high pressures, $K_S$ exhibits a monotonic increase in the investigated pressure range, while $G_S$ is essentially not sensitive to pressure. The high-pressure behavior of both aggregate moduli can be described using 3rd-order Eulerian finite strain equations (Stixrude & Lithgow-Bertelloni, 2005). The room pressure isotropic aggregate elastic moduli and their first pressure derivative resulting from the fitting are tabulated in Table 1, and presented in Figure 2a. Our results of $K^R_{S0} = 62.1(10)$ GPa and $K'^R_{S0} = 5.7(4)$ are different from the values ($K_0 = 52$ GPa, $K'_0 = 8.5$) resulting from the 3rd-order equation of state fit to the unit-cell volumes predicted by GGA-based calculations (Mookherjee & Capitani, 2011). This difference may be due to GGA overestimating unit-cell volumes, as discussed by Mookherjee and Capitani (2011). On the other hand, our results in better agreement with computational predictions at 300 K ($K_0 = 64.55$ GPa, $K'_0 = 6.94$, Capitani & Stixrude, 2012), and in perfect agreement with previous XRD investigations on powdered samples ($K_{T0} = 62(2)$ GPa and $K'_{T0} = 6.4(10)$, Hilairet et al., 2006), and single-crystal ($K_{T0} = 62.9(4)$ GPa and $K'_{T0} = 6.1(2)$, Nestola et al., 2010) of antigorite, supporting the robustness of our single-crystal elasticity data set. Comparison with literature shows that the GGA-derived $K^H$ from Mookherjee and Capitani (2011) diverges from ours at high

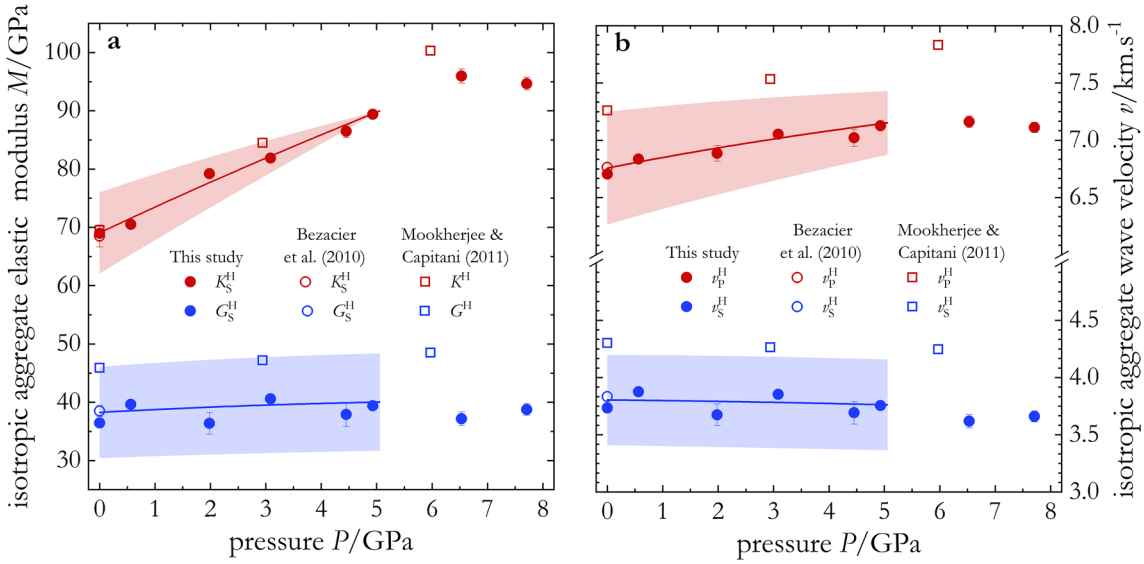


**Figure 2.** Isotropic aggregate elastic moduli (a) and velocities (b) of antigorite as function of pressure. Solid symbols are values obtained this study; open symbols are literature data. Solid lines are fits to our data up to $P_{ruby}$ = 5.17 GPa using 3rd-order finite strain equations (Text S3 in Supporting Information S1). Shadings in (a) and (b) show the full range between Voigt and Reuss bounds on the results from this study.

pressures, eventually exceeding the Voigt bound determined in the present study at $P > 3$ GPa. This difference is likely due to the stiffening of the $c_{11}$, $c_{22}$ and $c_{12}$ calculated in the GGA study for compression up to about 6 GPa, whereas the same $c_{ij}$ determined in this study show softening (Figure 1). On the other hand, the weak dependence on pressure observed in $G$ agrees well with computational predictions (Mookherjee & Capitani, 2011) (Table 1).

Isotropic aggregate compressional, $v_P = \sqrt{\frac{K_S + 4/3G}{\rho}}$, and shear, $v_S = \sqrt{\frac{G}{\rho}}$ wave velocities (Figure 2b) values determined at room pressure in this study match those determined by previous Brillouin spectroscopy experiments (Bezacier et al., 2010), while GGA predicts higher values for both velocities (Mookherjee & Capitani, 2011). Specifically, GGA-based Hill averaged values exceed the Voigt bound determined in this study. This is linked to the differences in isotropic aggregate moduli and their pressure derivative as mentioned above, and may be further enhanced by unit-cell volumes overestimation (i.e., smaller density than experiments at equivalent pressure) intrinsic to the GGA.

## 4. The Seismic Signature of Serpentinized Slabs

Seismically, serpentinized slabs may be distinguishable from dry slabs because of their characteristic S-wave anisotropy - a feature that has been directly attributed to the presence of antigorite-bearing rocks constituting the serpentinized fraction of slabs, as well as the hydrated mantle above most subduction zones (Faccenda et al., 2008).

Here, we use our experimental data to calculate the seismic properties of antigorite-bearing rocks at relevant pressures assuming different degrees of serpentinization. We use our results to estimate the potential shear wave anisotropy signature characterizing serpentinized slabs. In particular, we focus on the dependence of the shear wave splitting on the incidence angle $\beta$, a parameter defining the geometrical relation between the propagation direction of seismic waves and the orientation of the antigorite foliation plane in antigorite-bearing rocks. In our model, a seismic wave with zero degree incidence angle would be propagating parallel to the antigorite foliation plane, hence normal to the pre-existing lithospheric mantle olivine foliation plane (Morales et al., 2013). Our modeling relies on the high-pressure elasticity data set determined in this study with the CPO of antigorite determined by electron backscatter diffraction (EBSD) in a serpentinite from Val Malenco, Italy (Morales et al., 2018). Antigorite-bearing rocks were treated as mixtures between olivine and antigorite, and their seismic properties were determined through a self-consistent approach using the MATLAB software AnisEulerSC (Kim et al., 2020, see also: https://github.com/ekim1419/AnisEulerSC). Specifically, this code allows for the

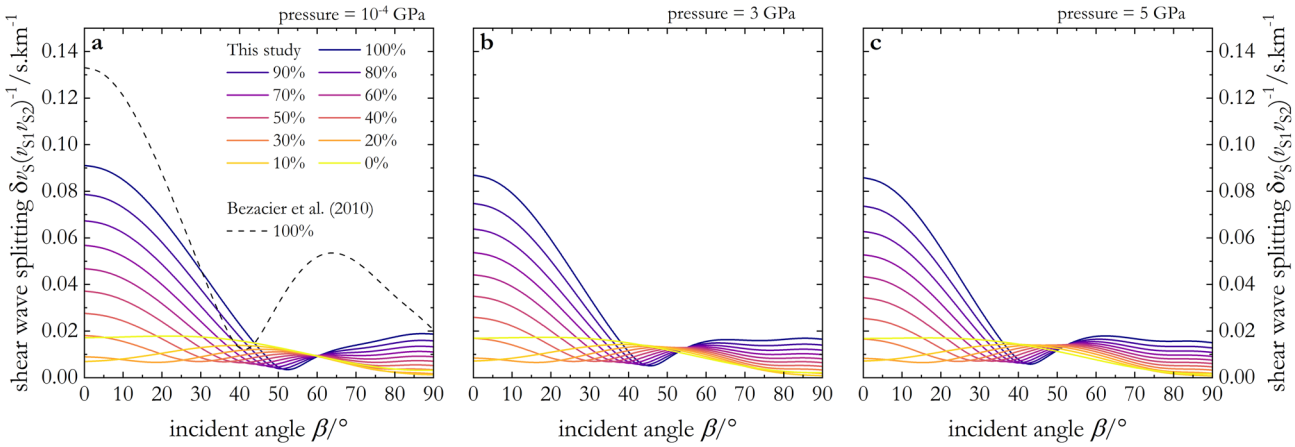


**Figure 3.** Shear wave splitting of antigorite-bearing rocks as function of the incident angle. Calculated values performed at room pressure, 3 and 5 GPa are reported in (a), (b) and (c) respectively. *Y*-axis range is shared. The legend shows the color scale used to distinguish modeled lithologies with different serpentinization rate. The legend reported in (a) applies to (b) and (c) as well. Solid lines show the value determined from the result on this study, while the dashed line shows literature results obtained for an entirely serpentinized rock.

implementation of multi-phase elasticity, grain shape constraints, and elastic inclusions. For the olivine input, we have modeled a "A-type" CPO using the unimodal Orientation Distribution Function (ODF) option of MTEX (https://mtex-toolbox.github.io/UnimodalODFs.html) and the aggregate elastic coefficients were calculated using results from single crystal measurements of Zha et al. (1998). Although olivine CPO may change considerably due to variations of stress conditions, temperature and water content (e.g., Jung et al., 2006), the A-type is by far the dominant olivine CPO observed in most tectonic environments (e.g., Tommasi & Vauchez, 2015). Different degrees of serpentinization were modeled by changing the ratio between olivine and antigorite, ranging from a dry dunite (100% olivine), to a fully serpentinized rock (100% antigorite), hence following a simplified approach that does not necessarily reflect realistic pre-hydration mantle composition. Calculations were performed at three different pressure points, covering the pressure range relevant for antigorite in subduction environments (Syracuse et al., 2010; Ulmer & Trommsdorff, 1995). No experimental constraints on the temperature effect on individual $c_{ij}$ are currently available. However, previous calculations within the quasi-harmonic approximation suggest temperature to have a relatively weak influence on the elasticity of antigorite (Bezacier et al., 2013). Hence, our modeling was limited to room temperature. Further details of the modeling are reported in Text S5 in Supporting Information S1, and input parameters are reported in Table S3 in Supporting Information S1.

According to our model, a fully serpentinized rock at room pressure exhibits maximum shear wave splitting (about 0.09 s/km) for seismic waves travelling parallel to the antigorite foliation plane (Figure 3). Therefore, an ~11-km path through a fully serpentinized antigorite-bearing body is needed to produce a 1 s delay of the slow shear wave, granted this is traveling parallel to the antigorite foliation. At room pressure (Figure 3a), our findings are in good qualitative agreement with previous calculations (Bezacier et al., 2010). However, our model suggests an absolute value that is about 30% lower than that previously determined (Bezacier et al., 2010). Also, we predict the shear wave splitting to show a high sensitivity to the incidence angle. An increase in incidence angle results in shear wave splitting decreasing rapidly as it approaches a local minimum at about 35–55° from the foliation-parallel direction. In the case of a fully serpentinized rock at room pressure, the modeled shear wave splitting reaches a local minimum of about 0.005 s/km at an incidence angle of ~53°. Therefore, our findings suggest that the shear wave anisotropy caused by a serpentinized slab largely changes through a mechanism independent of the serpentinization degree, providing an additional explanation for the spatial shear wave delay time variations detected by seismic waves sampling subducting slabs (e.g., Long & van der Hilst, 2005). Maximum and minimum shear wave splitting values exhibit a relatively weak sensitivity to pressure, hence suggesting that also temperature would have a negligible effect on shear-wave splitting in antigorite-bearing rocks. However, the minimum shifts toward lower incidence angle values as pressure is increased (~43° at 5 GPa). This suggests that spatial variation in shear wave delay times may be further enhanced at depth, being of particular relevance for slabs that show abrupt steepening while subducting, as for example, observed in the Tonga-Kermadek (Bonnardot et al., 2007), and Japan (Zhao et al., 1997) subduction systems. Also, our results show that sampling antigorite-bearing rocks

with relatively large incident angles would always lead to low shear wave delay times, independent of the serpentinization degree and/or pressure. This finding is important when interpreting shear wave delay times from vertical seismic waves traveling through steeply dipping slabs, such as the southern Mariana subduction zone (Miller et al., 2006).

Our model clearly shows that reducing the serpentinization degree, that is, the antigorite fraction in the modeled lithologies, suppresses maximum shear wave splitting, eventually leading the entire dispersion curve to collapse to values lower than 0.02 s/km at all investigated pressures. Interestingly, we note that for rocks having serpentinization degrees lower than 30%, the magnitude of shear wave splitting would be similar, or even lower, than those calculated for dry dunite (i.e., 100% olivine). This poses an important threshold for quantifying the serpentinization in slabs through the interpretation of shear wave delay times.

Ultimately, we note that the combined effect of incidence angle and serpentinization degrees possibly results in fully serpentinized rocks showing shear wave splitting values lower than dry dunites, hence considering seismic ray path is crucial when constraining serpentinization in slabs through the interpretation of shear wave delay times.

## Data Availability Statement

Acoustic wave velocity data used for $c_{ij}$ determination are available at https://doi.org/10.6084/m9.figshare.20348748. Elastic stiffness tensors of antigorite-bearing rocks are available at https://doi.org/10.6084/m9.figshare.20348781.

**Acknowledgments**
The authors thank R. Njul for sample polishing. N. S. acknowledges support by the IRTG "Deep Earth Volatile Cycles" (GRK 2156/1), and the European Union's Horizon 2020 research and innovation Programme (ERC grant 864877). A. K. acknowledges financial support provided by the DFG grant KU 3447/1.

## References

Bezacier, L., Reynard, B., Bass, J. D., Sanchez-Valle, C., & Van de Moortèle, B. (2010). Elasticity of antigorite, seismic detection of serpentinites, and anisotropy in subduction zones. *Earth and Planetary Science Letters*, *289*(1–2), 198–208. https://doi.org/10.1016/j.epsl.2009.11.009

Bezacier, L., Reynard, B., Cardon, H., Montagnac, G., & Bass, J. D. (2013). High-pressure elasticity of serpentine and seismic properties of the hydrated mantle wedge. *Journal of Geophysical Research: Solid Earth*, *118*(2), 527–535. https://doi.org/10.1002/jgrb.50076

Boehler, R., & De Hantsetters, K. (2004). New anvil designs in diamond-cells. *High Pressure Research*, *24*(3), 391–396. https://doi.org/10.1080/08957950412331323924

Bonnardot, M.-A., Régnier, M., Ruellan, E., Christova, C., & Tric, E. (2007). Seismicity and state of stress within the overriding plate of the Tonga-Kermadec subduction zone. *Tectonics*, *26*(5). https://doi.org/10.1029/2006TC002044

Campione, M., & Capitani, G. C. (2013). Subduction-zone earthquake complexity related to frictional anisotropy in antigorite. *Nature Geoscience*, *6*(10), 847–851. https://doi.org/10.1038/ngeo1905

Capitani, G. C., & Mellini, M. (2004). The modulated crystal structure of antigorite: The m = 17 polysome. *American Mineralogist*, *89*(1), 147–158. https://doi.org/10.2138/am-2004-0117

Capitani, G. C., & Mellini, M. (2005). HRTEM evidence for 8-reversals in the m = 17 antigorite polysome. *American Mineralogist*, *90*(5–6), 991–999. https://doi.org/10.2138/am.2005.1634

Capitani, G. C., & Mellini, M. (2006). The crystal structure of a second antigorite polysome (m = 16), by single-crystal synchrotron diffraction. *American Mineralogist*, *91*(2–3), 394–399. https://doi.org/10.2138/am.2006.1919

Capitani, G. C., & Stixrude, L. (2012). A first-principle investigation of antigorite up to 30 GPa: Structural behavior under compression. *American Mineralogist*, *97*(7), 1177–1186. https://doi.org/10.2138/am.2012.3956

Contreras-Reyes, E., Grevemeyer, I., Flueh, E. R., & Reichert, C. (2008). Upper lithospheric structure of the subduction zone offshore of southern Arauco Peninsula, Chile, at ~38°S. *Journal of Geophysical Research*, *113*(B7), B07303. https://doi.org/10.1029/2007JB005569

Contreras-Reyes, E., Grevemeyer, I., Watts, A. B., Flueh, E. R., Peirce, C., Moeller, S., & Papenberg, C. (2011). Deep seismic structure of the Tonga subduction zone: Implications for mantle hydration, tectonic erosion, and arc magmatism. *Journal of Geophysical Research*, *116*(B10), B10103. https://doi.org/10.1029/2011JB008434

De Shon, H. R., & Schwartz, S. Y. (2004). Evidence for serpentinization of the forearc mantle wedge along the Nicoya Peninsula, Costa Rica. *Geophysical Research Letters*, *31*(21). https://doi.org/10.1029/2004GL021179

Dewaele, A., Loubeyre, P., & Mezouar, M. (2004). Equations of state of six metals above 94 GPa. *Physical Review B*, *70*(9), 094112. https://doi.org/10.1103/PhysRevB.70.094112

Escartín, J., Hirth, G., & Evans, B. (1997). Effects of serpentinization on the lithospheric strength and the style of normal faulting at slow-spreading ridges. *Earth and Planetary Science Letters*, *151*(3), 181–189. https://doi.org/10.1016/S0012-821X(97)81847-X

Escartín, J., Hirth, G., & Evans, B. (2001). Strength of slightly serpentinized peridotites: Implications for the tectonics of oceanic lithosphere. *Geology*, *29*(11), 1023–1026. https://doi.org/10.1130/0091-7613(2001)029<1023:sosspi>2.0.co;2

Faccenda, M. (2014). Water in the slab: A trilogy. *Tectonophysics*, *614*, 1–30. https://doi.org/10.1016/j.tecto.2013.12.020

Faccenda, M., Burlini, L., Gerya, T. V., & Mainprice, D. (2008). Fault-induced seismic anisotropy by hydration in subducting oceanic plates. *Nature*, *455*(7216), 1097–1100. https://doi.org/10.1038/nature07376

Faccenda, M., Gerya, T. V., & Burlini, L. (2009). Deep slab hydration induced by bending-related variations in tectonic pressure. *Nature Geoscience*, *2*(11), 790–793. https://doi.org/10.1038/ngeo656

Ferrand, T. P., Hilairet, N., Incel, S., Deldicque, D., Labrousse, L., Gasc, J., et al. (2017). Dehydration-driven stress transfer triggers intermediate-depth earthquakes. *Nature Communications*, *8*(1), 15247. https://doi.org/10.1038/ncomms15247

Frost, D. J. (1999). The stability of dense hydrous magnesium silicates in Earth's transition zone and lower mantle. In *Mantle petrology: field observations and high pressure experimentation: A tribute to Francis R.(Joe) Boyd* (pp. 283–296). The Geochemical Society.

Haussühl, S. (2007). *Physical properties of crystals: An introduction*. Wiley-VCH.

Hilairet, N., Daniel, I., & Reynard, B. (2006). Equation of state of antigorite, stability field of serpentines, and seismicity in subduction zones. *Geophysical Research Letters*, *33*(2), L02302. https://doi.org/10.1029/2005GL024728

Hill, R. S. R. (1952). The elastic behaviour of a crystalline aggregate. *Proceedings of the Physical Society. Section B*, *65*(5), 349–354. https://doi.org/10.1088/0370-1298/65/5/307

Hirth, G., & Guillot, S. (2013). Rheology and tectonic significance of serpentinite. *Elements*, *9*(2), 107–113. https://doi.org/10.2113/gselements.9.2.107

Jung, H., Katayama, I., Jiang, Z., Hiraga, T., & Karato, S. (2006). Effect of water and stress on the lattice-preferred orientation of olivine. *Tectonophysics*, *421*(1), 1–22. https://doi.org/10.1016/j.tecto.2006.02.011

Kantor, I., Prakapenka, V., Kantor, A., Dera, P., Kurnosov, A., Sinogeikin, S., et al. (2012). BX90: A new diamond anvil cell design for X-ray diffraction and optical measurements. *Review of Scientific Instruments*, *83*(12), 125102. https://doi.org/10.1063/1.4768541

Kaproth, B. M., & Marone, C. (2013). Slow earthquakes, preseismic velocity changes, and the origin of slow frictional stick-slip. *Science*, *341*(6151), 1229–1232. https://doi.org/10.1126/science.1239577

Katayama, I., Hirauchi, K., Michibayashi, K., & Ando, J. (2009). Trench-parallel anisotropy produced by serpentine deformation in the hydrated mantle wedge. *Nature*, *461*(7267), 1114–1117. https://doi.org/10.1038/nature08513

Kern, H., Liu, B., & Popp, T. (1997). Relationship between anisotropy of P and S wave velocities and anisotropy of attenuation in serpentinite and amphibolite. *Journal of Geophysical Research*, *102*(B2), 3051–3065. https://doi.org/10.1029/96JB03392

Kim, E., Kim, Y., & Mainprice, D. (2020). AnisEulerSC: A MATLAB program combined with MTEX for modeling the anisotropic seismic properties of a polycrystalline aggregate with microcracks using self-consistent approximation. *Computers & Geosciences*, *145*, 104589. https://doi.org/10.1016/j.cageo.2020.104589

Klotz, S., Chervin, J.-C., Munsch, P., & Marchand, G. L. (2009). Hydrostatic limits of 11 pressure transmitting media. *Journal of Physics D: Applied Physics*, *42*(7), 075413. https://doi.org/10.1088/0022-3727/42/7/075413

Krantz, J. A., Parman, S. W., & Kelley, S. P. (2019). Recycling of heavy noble gases by subduction of serpentinite. *Earth and Planetary Science Letters*, *521*, 120–127. https://doi.org/10.1016/j.epsl.2019.06.007

Kurnosov, A., Kantor, I., Boffa-Ballaran, T., Lindhardt, S., Dubrovinsky, L., Kuznetsov, A., & Zehnder, B. H. (2008). A novel gas-loading system for mechanically closing of various types of diamond anvil cells. *Review of Scientific Instruments*, *79*(4), 045110. https://doi.org/10.1063/1.2902506

Long, M. D., & Silver, P. G. (2008). The subduction zone flow field from seismic anisotropy: A global view. *Science*, *319*(5861), 315–318. https://doi.org/10.1126/science.1150809

Long, M. D., & van der Hilst, R. D. (2005). Upper mantle anisotropy beneath Japan from shear wave splitting. *Physics of the Earth and Planetary Interiors*, *151*(3), 206–222. https://doi.org/10.1016/j.pepi.2005.03.003

Marquardt, H., Speziale, S., Koch-Müller, M., Marquardt, K., & Capitani, G. C. (2015). Structural insights and elasticity of single-crystal antigorite from high-pressure Raman and Brillouin spectroscopy measured in the (010) plane. *American Mineralogist*, *100*(8–9), 1932–1939. https://doi.org/10.2138/am-2015-5198

Mellini, M., Trommsdorff, V., & Compagnoni, R. (1987). Antigorite polysomatism: Behaviour during progressive metamorphism. *Contributions to Mineralogy and Petrology*, *97*(2), 147–155. https://doi.org/10.1007/bf00371235

Miller, M. S., Gorbatov, A., & Kennett, B. L. N. (2006). Three-dimensional visualization of a near-vertical slab tear beneath the southern Mariana arc. *Geochemistry, Geophysics, Geosystems*, *7*(6). https://doi.org/10.1029/2005GC001110

Moody, J. B. (1976). Serpentinization: A review. *Lithos*, *9*(2), 125–138. https://doi.org/10.1016/0024-4937(76)90030-x

Mookherjee, M., & Capitani, G. C. (2011). Trench parallel anisotropy and large delay times: Elasticity and anisotropy of antigorite at high pressures. *Geophysical Research Letters*, *38*(9), 2011GL047160. https://doi.org/10.1029/2011GL047160

Mookherjee, M., & Steinle-Neumann, G. (2009a). Detecting deeply subducted crust from the elasticity of hollandite. *Earth and Planetary Science Letters*, *288*(3), 349–358. https://doi.org/10.1016/j.epsl.2009.09.037

Mookherjee, M., & Steinle-Neumann, G. (2009b). Elasticity of phase-X at high pressure. *Geophysical Research Letters*, *36*(8), L08307. https://doi.org/10.1029/2009GL037782

Morales, L. F. G., Mainprice, D., & Boudier, F. (2013). The influence of hydrous phases on the microstructure and seismic properties of a hydrated mantle rock. *Tectonophysics*, *594*, 103–117. https://doi.org/10.1016/j.tecto.2013.03.022

Morales, L. F. G., Mainprice, D., & Kern, H. (2018). Olivine-antigorite orientation relationships: Microstructures, phase boundary misorientations and the effect of cracks in the seismic properties of serpentinites. *Tectonophysics*, *724–725*, 93–115. https://doi.org/10.1016/j.tecto.2017.12.009

Nestola, F., Angel, R. J., Zhao, J., Garrido, C. J., Sánchez-Vizcaíno, V. L., Capitani, G., & Mellini, M. (2010). Antigorite equation of state and anomalous softening at 6 GPa: An in situ single-crystal X-ray diffraction study. *Contributions to Mineralogy and Petrology*, *160*(1), 33–43. https://doi.org/10.1007/s00410-009-0463-9

Nye, J. F. (1985). *Physical properties of crystals: Their representation by tensors and matrices*. Oxford University Press.

Ohtani, E. (2020). The role of water in Earth's mantle. *National Science Review*, *7*(1), 224–232. https://doi.org/10.1093/nsr/nwz071

Padrón-Navarta, J. A., Tommasi, A., Garrido, C. J., & López Sánchez-Vizcaíno, V. (2012). Plastic deformation and development of antigorite crystal preferred orientation in high-pressure serpentinites. *Earth and Planetary Science Letters*, *349*(350), 75–86. https://doi.org/10.1016/j.epsl.2012.06.049

Ranero, C. R., Phipps Morgan, J., McIntosh, K., & Reichert, C. (2003). Bending-related faulting and mantle serpentinization at the Middle America trench. *Nature*, *425*(6956), 367–373. https://doi.org/10.1038/nature01961

Ranero, C. R., & Sallarès, V. (2004). Geophysical evidence for hydration of the crust and mantle of the Nazca plate during bending at the north Chile trench. *Geology*, *32*(7), 549–552. https://doi.org/10.1130/G20379.1

Rupke, L. (2004). Serpentine and the subduction zone water cycle. *Earth and Planetary Science Letters*, *223*(1–2), 17–34. https://doi.org/10.1016/j.epsl.2004.04.018

Schmidt, M. W., & Poli, S. (1998). Experimentally based water budgets for dehydrating slabs and consequences for arc magma generation. *Earth and Planetary Science Letters*, *163*(1–4), 361–379. https://doi.org/10.1016/S0012-821X(98)00142-3

Schulze, K., Buchen, J., Marquardt, K., & Marquardt, H. (2017). Multi-sample loading technique for comparative physical property measurements in the diamond-anvil cell. *High Pressure Research*, *37*(2), 159–169. https://doi.org/10.1080/08957959.2017.1299719

Schwartz, S., Guillot, S., Reynard, B., Lafay, R., Debret, B., Nicollet, C., et al. (2013). Pressure–temperature estimates of the lizardite/antigorite transition in high pressure serpentinites. *Lithos*, *178*, 197–210. https://doi.org/10.1016/j.lithos.2012.11.023

Sibson, R. H. (2000). Fluid involvement in normal faulting. *Journal of Geodynamics*, *29*(3), 469–499. https://doi.org/10.1016/S0264-3707(99)00042-3

Smith, E. M., Ni, P., Shirey, S. B., Richardson, S. H., Wang, W., & Shahar, A. (2021). Heavy iron in large gem diamonds traces deep subduction of serpentinized ocean floor. *Science Advances*, *7*(14), eabe9773. https://doi.org/10.1126/sciadv.abe9773

Stixrude, L., & Lithgow-Bertelloni, C. (2005). Thermodynamics of mantle minerals—I. Physical properties. *Geophysical Journal International*, *162*(2), 610–632. https://doi.org/10.1111/j.1365-246X.2005.02642.x

Syracuse, E. M., van Keken, P. E., & Abers, G. A. (2010). The global range of subduction zone thermal models. *Physics of the Earth and Planetary Interiors*, *183*(1), 73–90. https://doi.org/10.1016/j.pepi.2010.02.004

Tommasi, A., & Vauchez, A. (2015). Heterogeneity and anisotropy in the lithospheric mantle. *Tectonophysics*, *661*, 11–37. https://doi.org/10.1016/j.tecto.2015.07.026

Trots, D. M., Kurnosov, A., Boffa Ballaran, T., Tkachev, S., Zhuravlev, K., Prakapenka, V., et al. (2013). The Sm:YAG primary fluorescence pressure scale. *Journal of Geophysical Research: Solid Earth*, *118*(11), 5805–5813. https://doi.org/10.1002/2013JB010519

Ulmer, P., & Trommsdorff, V. (1995). Serpentine stability to mantle depths and subduction-related magmatism. *Science*, *268*(5212), 858–861. https://doi.org/10.1126/science.268.5212.858

Watt, J. P. (1987). POLYXSTAL: A FORTRAN program to calculate average elastic properties of minerals from single-crystal elasticity data. *Computers & Geosciences*, *13*(5), 441–462. https://doi.org/10.1016/0098-3004(87)90050-1

Zha, C.-S., Duffy, T. S., Downs, R. T., Mao, H., & Hemley, R. J. (1998). Brillouin scattering and X-ray diffraction of San Carlos olivine: Direct pressure determination to 32 GPa. *Earth and Planetary Science Letters*, *159*(1), 25–33. https://doi.org/10.1016/s0012-821x(98)00063-6

Zhao, D., Matsuzawa, T., & Hasegawa, A. (1997). Morphology of the subducting slab boundary in the northeastern Japan arc. *Physics of the Earth and Planetary Interiors*, *102*(1), 89–104. https://doi.org/10.1016/S0031-9201(96)03258-X

## References From the Supporting Information

Angel, R. J. (2000). Equations of state. *Reviews in Mineralogy and Geochemistry*, *41*(1), 35–59. https://doi.org/10.2138/rmg.2000.41.2

Birch, F. (1947). Finite elastic strain of cubic crystals. *Physical Review*, *71*(11), 809–824. https://doi.org/10.1103/PhysRev.71.809

Eshelby, J. D. (1957). The determination of the elastic field of an ellipsoidal inclusion, and related problems. *Proceedings of the Royal Society of London. Series A. Mathematical and Physical Sciences*, *241*(1226), 21. https://doi.org/10.1098/rspa.1957.0133

Ghaderi, N., Zhang, H., & Sun, T. (2015). Relative stability and contrasting elastic properties of serpentine polymorphs from first-principles calculations. *Journal of Geophysical Research: Solid Earth*, *120*(7), 4831–4842. https://doi.org/10.1002/2015JB012148

Hielscher, R., & Schaeben, H. (2008). A novel pole figure inversion method: Specification of the MTEX algorithm. *Journal of Applied Crystallography*, *41*(6), 1024–1037. https://doi.org/10.1107/S0021889808030112

Kurnosov, A., Marquardt, H., Frost, D. J., Boffa Ballaran, T., & Ziberna, L. (2017). Evidence for a Fe 3+ -rich pyrolitic lower mantle from (Al, Fe)-bearing bridgmanite elasticity data. *Nature*, *543*(7646), 543–546. https://doi.org/10.1038/nature21390

Lindsay, S. M., Anderson, M. W., & Sandercock, J. R. (1981). Construction and alignment of a high performance multipass vernier tandem Fabry–Perot interferometer. *Review of Scientific Instruments*, *52*(10), 1478–1486. https://doi.org/10.1063/1.1136479

Mainprice, D. (1990). A FORTRAN program to calculate seismic anisotropy from the lattice preferred orientation of minerals. *Computers & Geoscience*, *16*(3), 385–393. https://doi.org/10.1016/0098-3004(90)90072-2

Mainprice, D. (1997). Modelling the anisotropic seismic properties of partially molten rocks found at mid-ocean ridges. *Tectonophysics*, *279*(1), 161–179. https://doi.org/10.1016/S0040-1951(97)00122-4

Rigaku Oxford Diffraction. (2015). *CrysAlis PRO*. Rigaku Oxford Diffraction.

Sandercock, J. R. (1982). *Trends in brillouin scattering: Studies of opaque materials, supported films, and central modes* (pp. 173–206). Springer. https://doi.org/10.1007/3540115137_6

Whitfield, C. H., Brody, E. M., & Bassett, W. A. (1976). Elastic moduli of NaCl by Brillouin scattering at high pressure in a diamond anvil cell. *Review of Scientific Instruments*, *47*(8), 942–947. https://doi.org/10.1063/1.1134778

Willis, J. R. (1977). Bounds and self-consistent estimates for the overall properties of anisotropic composites. *Journal of the Mechanics and Physics of Solids*, *25*(3), 185–202. https://doi.org/10.1016/0022-5096(77)90022-9

Yang, C., Inoue, T., Yamada, A., Kikegawa, T., & Ando, J. (2014). Equation of state and phase transition of antigorite under high pressure and high temperature. *Physics of the Earth and Planetary Interiors*, *228*, 56–62. https://doi.org/10.1016/j.pepi.2013.07.008

Zha, C.-S., Duffy, T. S., Downs, R. T., Mao, H.-K., & Hemley, R. J. (1996). Sound velocity and elasticity of single-crystal forsterite to 16 GPa. *Journal of Geophysical Research*, *101*(B8), 17535–17545. https://doi.org/10.1029/96JB01266